2018

Thermal Radiation Measurement and Development of Tunable Plasmonic Thermal Emitter Using Strain-induced Buckling in Metallic Layers

Amir Kazemi-Moridani

الـمـنـارة للاستشارات

www.manaraa.com

THERMAL RADIATION MEASUREMENT AND DEVELOPMENT OF TUNABLE PLASMONIC THERMAL EMITTER USING STRAIN-INDUCED BUCKLING IN METALLIC LAYERS

A Thesis Presented

by

AMIR KAZEMI-MORIDANI

Submitted to the Graduate School of the
University of Massachusetts Amherst in partial fulfillment
of the requirements for the degree of

MASTER OF SCIENCE in MECHANICAL ENGINEERING

September 2018

Department of Mechanical and Industrial Engineering

THERMAL RADIATION MEASUREMENT AND DEVELOPMENT OF TUNABLE PLASMONIC THERMAL EMITTER USING STRAIN-INDUCED BUCKLING IN METALLIC LAYERS

A Thesis Presented

by

AMIR KAZEMI-MORIDANI

Approved as to style and content by:

_____
Jae-Hwang Lee, Chair

_____
Jonathan P. Rothstein, Member

_____
Stephen Nonnenmann, Member

_____
Sundar Krishnamurty,
Department Head
Department of Mechanical and Industrial
Engineering

DEDICATION

To Mina, without whom, all of this would lose value

and

My parents, Fatemeh and Naghi, who taught me how to live joyfully.

ACKNOWLEDGMENTS

ABSTRACT

THERMAL RADIATION MEASUREMENT AND DEVELOPMENT OF TUNABLE PLASMONIC THERMAL EMITTER USING STRAIN-INDUCED BUCKLING IN METALLIC LAYERS

SEPTEMBER 2018

AMIR KAZEMI-MORIDANI, B.S., AMIRKABIR UNIVERSITY OF TECHNOLOGY

M.S.M.E, UNIVERSITY OF MASSACHUSETTS AMHERST

Directed by: Professor Jae-Hwang Lee

An infrared radiometry setup has been developed based on a commercially available FTIR spectrometer for measuring mid-infrared thermal radiation. The setup was calibrated with a lab-built blackbody source. The setup was tested with a grating structure with 4-micron periodicity. Periodic microstructures using nickel and gold are fabricated on elastomeric substrates by use of strain-induced buckling of the nickel layer. The intrinsically low emissivity of gold in the mid-infrared regime is selectively enhanced by the surface plasmonic resonance at three different mid-infrared wavelengths, 4.5 µm, 6.3 µm, and 9.4 µm. As the thermal emission enhancement effect exists only for the polarization perpendicular to the orientation of the microstructures, substantially polarized thermal emission with an extinction ratio of close to 3 is demonstrated. Moreover, the elastically deformed plasmonic thermal emitters demonstrate strain-dependent emission peaks, which can be applied for future mechano-thermal sensing and dynamic thermal signature modulation.

TABLE OF CONTENTS

LIST OF FIGURES

ix

CHAPTER 1

GENERAL INTRODUCTION

1.1 Introduction

Manipulation of light by exploiting the light-matter interaction has been a major field of research in the modern science. Surface plasmon polaritons are electromagnetic excitations that are guided by a metal–dielectric interface that are extremely confined in the perpendicular direction i.e. they vanish evanescently in the perpendicular direction.[1]–[4] As compared to conventional optical applications, where the smallest attainable size is almost always limited by the wavelength of the radiation, [5]–[8] we will study the enhancement of thermal radiation by coupling surface plasmon polaritons to propagating modes of electromagnetic radiations by introducing dynamically tunable microstructures at the metal-dielectric interface. [9]–[13]

1.2 Thermal Radiation

Any object with a temperature above the absolute zero emits electromagnetic radiations. An ideal emitter does not reflect any light and in a state of equilibrium absorbs all the incident energy and emits its own energy with a temperature-dependent characteristic spectrum that is known as blackbody radiation. One of the major unsolved problems near the end of the nineteenth century was the derivation of blackbody spectrum from fundamental physical principles.[14] Lord Rayleigh had attempted to explain

1

blackbody radiation by using Maxwell's equations and the fundamentals of thermal physics. His attempt could explain the behavior of blackbody for long wavelength but would result in infinite values as wavelength approached to zero. Wien had also found an empirical relation with two constants for blackbody radiation at shorter wavelengths and the constants could be calculated for the best fit to experimental data. Later, German physicist Max Planck was successful in modifying the Wien's expression to match with the Rayleigh's prediction, and this modified expression would fit the blackbody spectrum at both ends. In an attempt to explain his new expression, Planck used a mathematical trick that energy of a standing electromagnetic wave with wavelength λ cannot have any arbitrary amount of energy and the energy should be a value that is integral multiples of a minimum wave energy, called a quantum of energy. This quantum of energy is given by hc/λ where h is the Planck's constant. With this assumption, an object at low temperatures could not provide enough energy to reach the required minimum energy for an arbitrarily short wavelength wave.[14] The spectrum of this radiation is described by Planck's law, B_λ is the spectral radiance per wavelength:

$$B_\lambda(\lambda, T) = \frac{2hc^2}{\lambda^5} \frac{1}{e^{\frac{hc}{\lambda k_B T}} - 1} \quad (W \cdot sr^{-1} \cdot m^{-3}) \tag{1}$$

Where T is the temperature, h is the Planck's constant, c is the speed of light, λ is the wavelength of the emitted electromagnetic radiation, and k_B is the Boltzmann constant. The total radiation emitted from a blackbody only depends on the temperature of the object.

2

Part of this electromagnetic radiation in the wavelength range of 700 nm to 1 mm is known as the infrared radiation. At the temperatures present in the Earth's atmosphere almost the entire electromagnetic radiation falls in the infrared range.

1.3 Surface Plasmon Polaritons at Metal-Dielectric Interface

Let's consider a flat interface between a non-absorbing dielectric in the z < 0 half-space (medium 1) with a positive dielectric constant ε_1 and a metal in the z > 0 half-space (medium 2) with a complex dielectric function $\varepsilon_2(\omega)$ (the real part of ε_2 is negative for metals) where ω is the frequency of light.[15] A schematic of the interface and the surface plasmon polariton with an evanescent amplitude of the electric field (in red) is shown in Figure 1. Now we will consider surface wave solutions that are confined to the interface. These waves show evanescent decay in the z-direction. Surface plasmon polaritons can only exist with the transverse magnetic polarization (magnetic field parallel to the interface). [16]
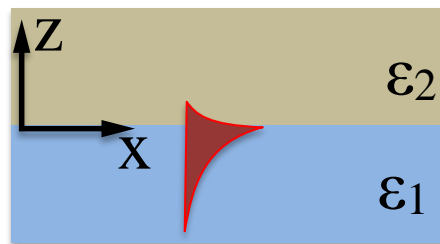
Figure 1- Schematic of metal (2)-dielectric (1) interface and the surface plasmon excitation at the interface

For the transverse magnetic polarization, without any loss of generality and to have simpler equations, we can assume that these waves are propagating in the x-direction. We can write:

$$E_i = \left(E_{i_x}, 0, E_{i_z}\right)e^{-\beta_i|z|}e^{i(k_i x - \omega t)} \tag{2}$$

$$H_i = \left(0, H_{i_y}, 0\right)e^{-\beta_i|z|}e^{i(k_i x - \omega t)} \tag{3}$$

Where index i represents the medium and β_i is the magnitude of the wave vector.[16] By substituting these equations into Maxwell's equations that are shown below:

$$\nabla \times E_i = -\frac{1}{c}\frac{\partial}{\partial t} H_i \tag{4}$$

$$\nabla \times H_i = \epsilon_i \frac{1}{c}\frac{\partial}{\partial t} E_i \tag{5}$$

$$\nabla . (\epsilon_i E_i) = 0 \tag{6}$$

$$\nabla . H_i = 0 \tag{7}$$

And applying the boundary conditions at the interface (components of E and H parallel to the interface must be continuous at the interface), we will arrive at:

$$k_1 = k_2 = k(\omega) = \frac{\omega}{c}\sqrt{\frac{\epsilon_1 \epsilon_2}{\epsilon_1 + \epsilon_2}} \tag{8}$$

In case of vacuum and a Drude semi-infinite metal with negligible collision frequency, we will have:

4

$$\epsilon_1 = 1, \epsilon_2 = 1 - \frac{\omega_p^2}{\omega^2} \tag{9}$$

$$k(\omega) = \frac{\omega}{c} \sqrt{\frac{\omega^2 - \omega_p^2}{2\omega^2 - \omega_p^2}} \tag{10}$$

Where ω_p shows the plasma frequency of the metal. [9], [17] Examples of the dispersion relaitons at the interface between Drude metal and air and Drude metal and silica are shown in Figure 2 from Reference [16].
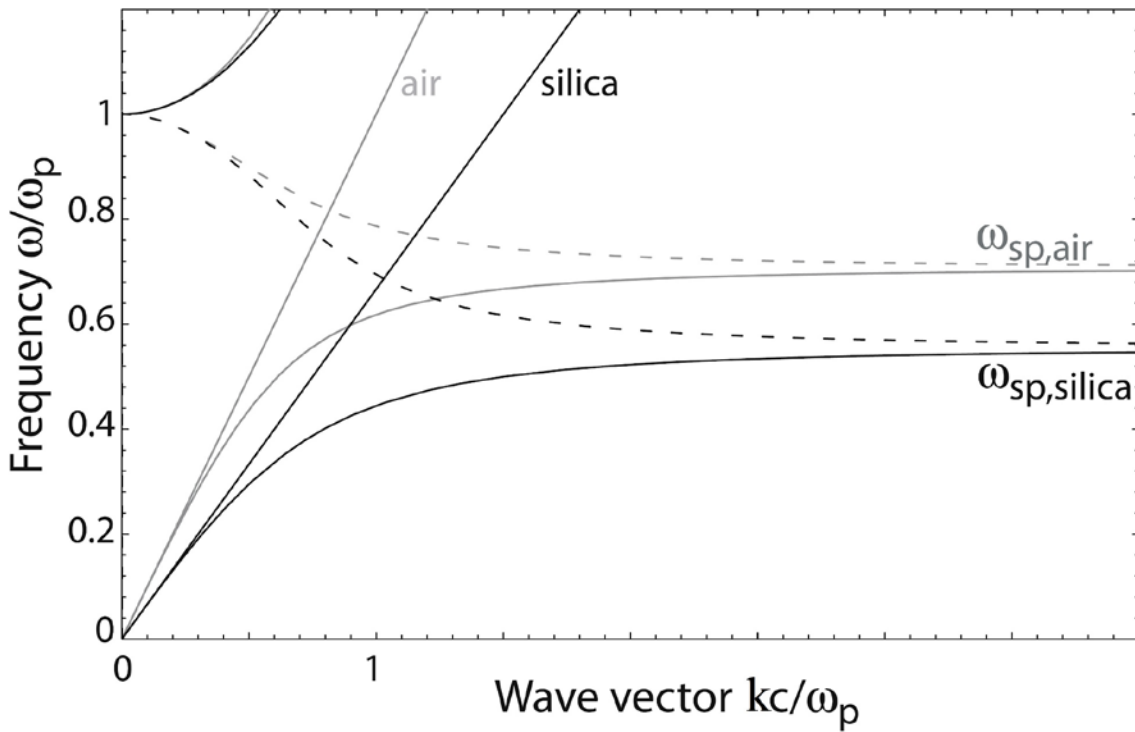
Figure 2- Dispersion relation for Surface Plasmon Polaritons at the interface between Drude metal and air and silica [16]

Figure 2 shows that a wavevector is not a linear function of the frequency for surface plasmon polaritons and always lies outside the cone of dielectric (in free space of homogeneous dielectrics the wavevector of plane waves depends linearly on the frequency)

[18]. This means that surface plasmon polaritons cannot couple to propagating modes of the dielectric due to a mismatch in momentum. However, there are several ways that allow coupling between propagating modes of radiation and surface plasmon polaritons. For example, a thin layer of metal on a prism made of glass would allow the surface plasmon polaritons at the metal-air interface to couple with the propagating modes in glass. As an example, it is shown in Figure 1 that for a range of k values, the dispersion curve of surface plasmon polaritons at metal-air interface lies inside the dielectric cone of the silica that means the surface plasmon polaritons at metal-air interface can be coupled to propagating modes in silica by using a thin layer of metal.

1.4 Coupling of surface plasmon polaritons by gratings

Coupling surface plasmon polariton modes to light can also be achieved by diffraction at a grating surface when the momentum matching condition (Equation 11) is satisfied:[16], [19]

$$k = k_p \sin \theta + ng \qquad (11)$$

Where k_p is the momentum of the incident photons, θ is the angle between light ray and the grating plane, g is the reciprocal vector of the grating (2π/periodicity) and n is an integer (1,2,3,…) representing the diffraction mode.[20]–[22]

The dispersion relation of a surface plasmon polariton at a corrugated interface is shown in Figure 3 from Reference [15]. The surface plasmon polariton dispersion curve has now been replicated inside the light line. This replication means that coupling can happen between light and surface plasmon polaritons with the help of a grating.[9] It is also interesting to note that a gap opens up where the different scattered SPP modes cross. The geometry (cross-section) of the grating determines the strength of the scattering/coupling.[23] Figure 3 shows that in addition to giving the possibility of coupling between light and surface plasmon polaritons, periodic structures also introduce band-gaps in the propagation of surface plasmon polaritons.[21], [24]
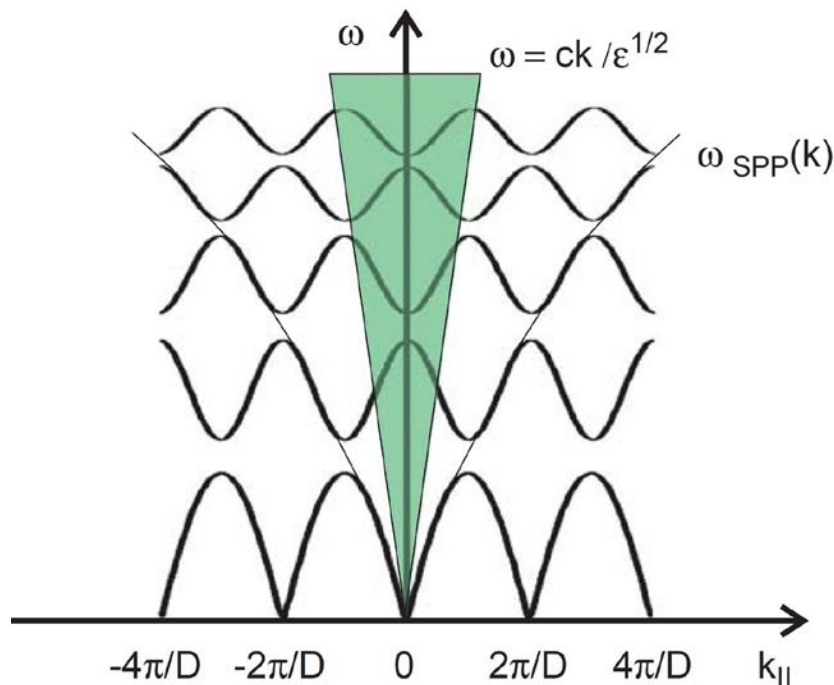
Figure 3- Surface plasmon polarinton dispersion on a periodic structure (periodicity = D) and formation of bandgaps. The dispersion relation on a flat surface is shown by the thin solid line. [15]

7

CHAPTER 2

METHODS

2.1 Strain-Induced Buckling

Formation of complex ordered structures induced by buckling of thin metallic sheets on an elastomeric substrate (Polydimethylsiloxane) has been reported previously.[25]–[27] In this work, we have used this method for making periodic tunable thermal emitters. The periodicity of the wrinkle depends on the mechanical properties of the substrate and the metallic layer as well as the thickness of the layer. We have used a Polydimethylsiloxane (PDMS) polymer system from the Dow Company called Sylgard 184® as an elastomeric substrate. 1-mm-thick strips of PDMS with a 1:10 ratio of the crosslinking agent to the polymer base by curing at 200° C for one hour have been prepared. Due to the preferable optical properties[28] of gold such as low absorption and high conductivity and its remarkable stability in air and high temperatures, we have attempted to make the samples by depositing gold on the elastomeric substrates. The target periodicity for mid-IR radiation enhancement given the capabilities of our radiation measurement setup should fall in the range of 4 to 10 μm.[29]–[31] As it is shown in Equation (12)

$$\Lambda = 2\pi d \left[\frac{(1 - v_s^2)E_f}{3(1 - v_f^2)E_s} \right]^{\frac{1}{3}} \tag{12}$$

We can have an estimate of the periodicity $\varLambda$ by using the elastic moduli of the metallic layer and PDMS, E_f and E_s, and Poisson's ratios of metal and PDMS, ν_f and ν_s. Given the low elastic modulus of gold, we were not able to make structures with the desired periodicity. Of course, an easy solution to this problem is increasing the thickness of the metallic layer, but the regularity of the pattern would be influenced by thicker metallic layers and thicker metallic layers would reduce the repeatability of the patterns. In order to fix this issue, we introduced another metallic layer for generating the desired periodicity. We have used nickel as the metallic layer to achieve the desired periodicities and sputter-coated the structure made from the nickel layer with a layer of gold to take advantage of the superior radiation properties of gold.

2.2 FTIR Radiometry

The radiation measurements were performed by a setup, which was developed in our lab based on a Fourier transform infrared (FTIR) spectrometer. FTIR spectroscopy is a well-known technique for studying the absorption/emission of materials and identification of molecules/chemical bonds in a sample based on their characteristic peaks.[32], [33] When infrared radiation passes through a thin slice of a material, part of the radiation will be absorbed by the material and the absorption spectrum of the sample can be studied by recording the radiation after passing through the sample.[34], [35] Most FTIR spectrometers use an interferometer.[36] There is a beamsplitter inside the interferometer

that divides the incoming infrared beam into two beams. One beam is directed toward a

fixed mirror while the other beam is directed toward a moving mirror (an amplitude of

movement is around a few millimeters). Figure 4 shows a schematic of a Michelson

interferometer which is used in the Nicolet 6700 FTIR spectrometer.
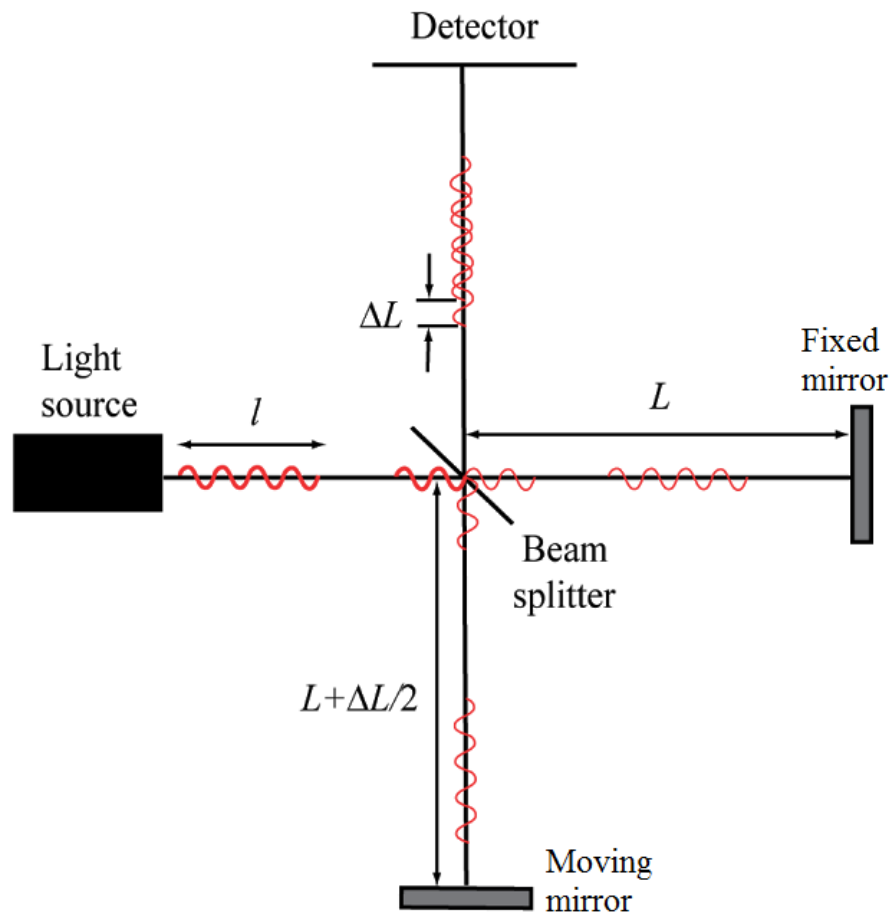
Figure 4- Michelson Interferometer

After reflecting off of the two mirrors the beams will be recombined at the

beamsplitter and directed toward the detector. Because of the path length difference of the

two beams, the beams will interfere with each other and generate a pattern that is known

as an interferogram. The interferogram combined with the position information of the

moving mirror can be used to extract radiation intensity for different infrared

frequencies.[37], [38] The information from the interferogram can be decoded to

wavevector domain via Fourier Transformation.[36] Figure 5 shows a few examples of

interferograms and their corresponding radiation spectra.[39]
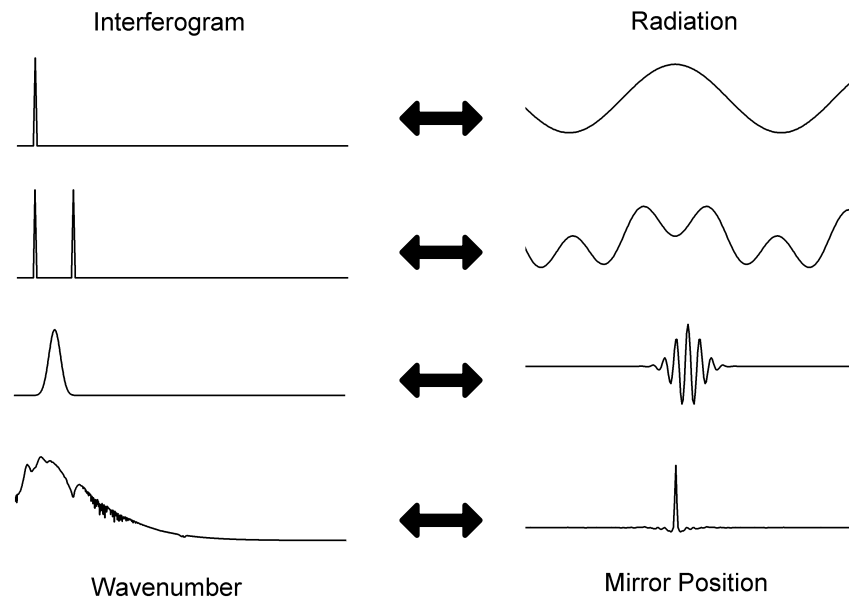
Figure 5- Interferograms and corresponding radiation spectra based on FFT [39]

In order to measure thermal radiation of the samples, we have removed one of the

mirrors from the FTIR spectrometer and used an external window on the frame of the

device for redirecting radiation from the source that is placed outside the system toward

11

the interferometer. The modified configuration of the measurement setup is shown in Figure 6.
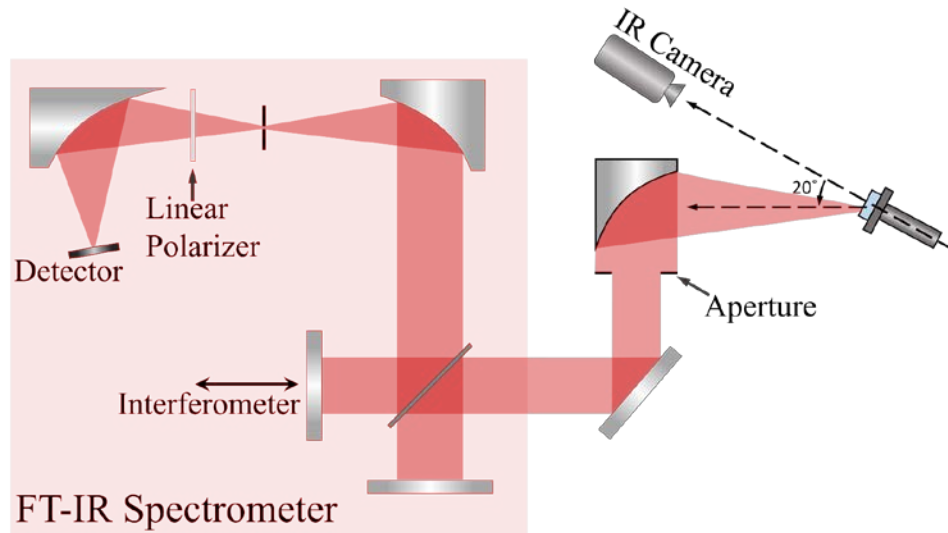
Figure 6 Schematic of the measurement setup

2.2.1 Blackbody Calibration

For calculating emissivity of the sample, we have calibrated the radiation measurement setup with a blackbody source. We have proposed a simple mathematical model for describing the radiation that is measured with the radiometry setup to calibrate our setup. In our model, the total radiation is the sum of radiation from the sample and a constant term that accounts for the background radiation. In Equation (13) for the calibration of the radiometry setup, *E* is the measured radiation signal, *BG* shows the

background contribution, R is the response function of the radiometry system which is a function of wavelength and BB is the blackbody radiation according to Planck's equation which is a function of wavelength and the temperature.

$$E(\lambda, T) = R(\lambda) [BG(\lambda) + BB(\lambda, T)] \tag{13}$$

In Equation (13), the response function and the background radiation are the unknowns, therefore by measuring the radiation of the blackbody at two different temperatures, we can solve a system of two equations for the two unknowns and determine the background contribution and the response function of the system. Examples of the calibration functions are shown in Figure 7. The absorption lines in the 1200 to 1800 cm^{-1} range originate from absorption spectrum of water vapor in air.[40] The features near 2350 cm^{-1} originate from the absorption characteristic lines of CO_2. [41] The noise features in
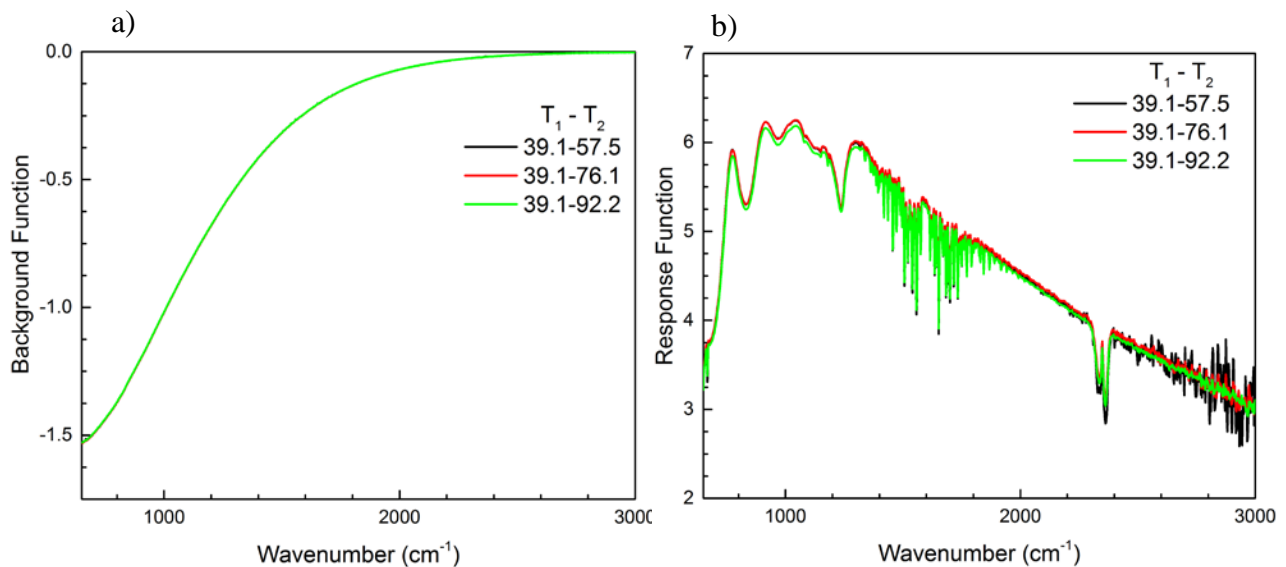
Figure 7- Example of a) background and b) response functions for blackbody calibration

13

the low-temperature calibration curve near the large wavenumber end of the graph are from weak radiation signals at low temperatures in that region.

The validity of this assumption can be verified by measuring the blackbody radiation at a different temperature (other than the temperatures used for calibration) and comparing the prediction of the equation with the measured spectrum of the blackbody at that temperature. Our system has shown less than 1% error in blackbody radiation measurement. Comparison of blackbody radiation based on the calibration and measurement with our system and the error of calibration are shown in Figure 8. The dashed curves show the measured blackbody radiation spectra with our system and the transparent solid curves show the radiation spectra based on Planck's equation. As it is shown in the left plot, the signal is very weak for larger wavenumbers (>2000 cm^{-1}). The weak signal results in high relative error in the calibration functions for short wavelengths.
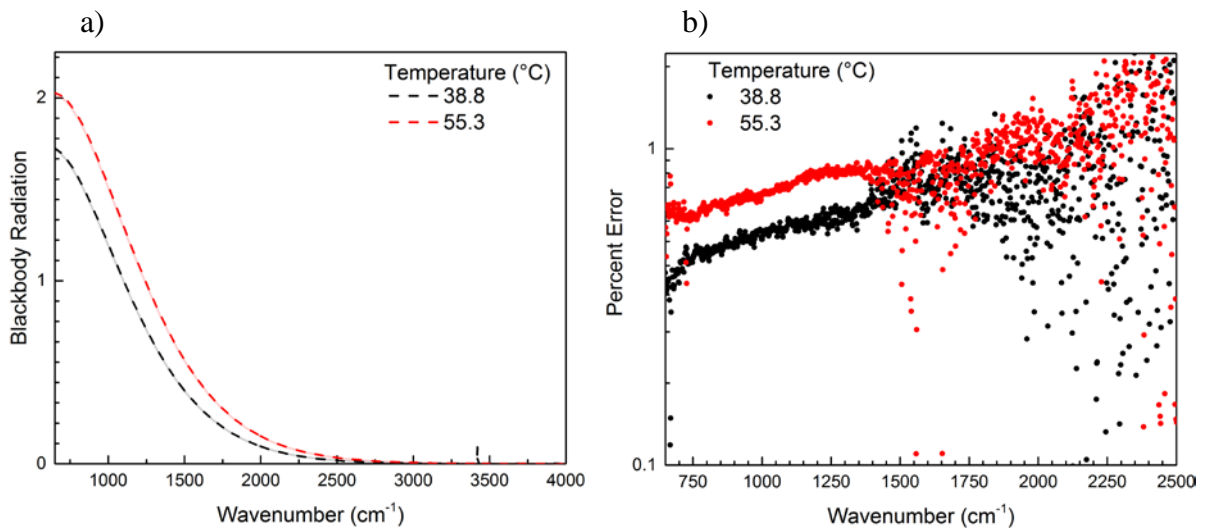
Figure 8- a) calibration comparison with Planck's equation and b) the plot of relative error

14

2.2.2 Nonlinearity of Mercury Cadmium Telluride Detector

In order to detect the thermal signals at low temperatures (room temperature – 250°C) we used a high sensitivity mercury cadmium telluride (MCT) detector that requires liquid nitrogen to be cooled down. The detectivity of common infrared detectors are shown in Figure 9 from reference. [42] We have used an MCT-A detector in our setup that has the highest detectivity for mid-infrared detectors that almost cover the entire mid-IR range.[42]
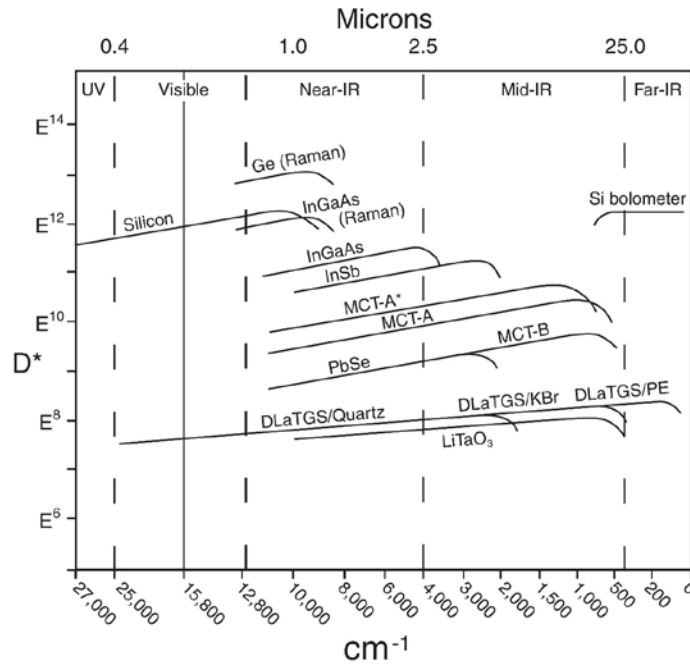
Figure 9- Detectivity of commercially available infrared detectors [42]

Detectors with high detectivities (D^*) exhibit nonlinearity in high radiation flux experiments. Equation (14) shows the dependency of D^* on bandwidth (Δf), detector area

(*A*), detector signal (*Vs*), the root mean square detector noise (*V_n*) and the energy flux at the detector (*E_s*).[42], [43]

$$D^* = \frac{\Delta f^{\frac{1}{2}} V_s}{V_n E_s A^{\frac{1}{2}}} \tag{14}$$

We have confirmed that our initial radiometry setup has a nonlinear response for radiation flux of our blackbody at room temperature. In order to eliminate the nonlinearity, we have implemented an aperture and a perforated sheet on the path of the infrared beam to reduce the radiation flux that reaches the detector. By controlling the radiation flux, we have changed the response of the detector to an almost linear response. The linearity of the detector's response can be verified by calibrating the system at different temperatures. Having the same results for the response functions (calibrated at different temperature pairs) shows that the detectivity does not depend on the income radiation flux (shown in Figure 7).

2.2.3 Sample Orientation

The FTIR spectrometer uses an interferometer, part of this modulated signal will leak out of the spectrometer. The modulated signal that leaves the spectrometer can be reflected at the sample's surface and be redirected toward the spectrometer once more. This reflection can introduce significant artifacts in the measured radiation spectrum. In order to avoid this issue, the samples were mounted at a tilted angle so that the reflection of the

modulated signal from the spectrometer will be redirected toward outside the surroundings.

A schematic of this configuration is shown in Figure 10.
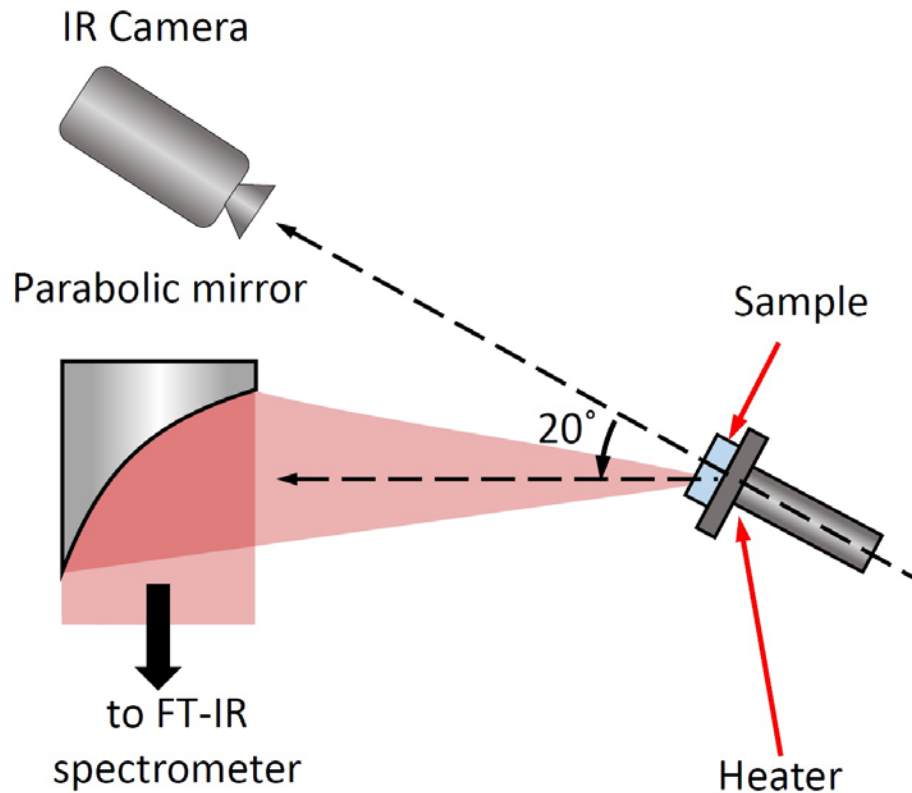
Figure 10- Orientation of the sample and camera relative to the spectrometer

2.3 Optical Profilometry

For determining the amplitude and periodicity of our structures, we have used an optical profilometer (Nexview, ZYGO).[44], [45] Optical profilometry is a well-known technique for determining the surface roughness and profiles of highly reflective surfaces. Optical profilometers use the interference pattern of light to detect the height profile of a

17

surface. A laser beam is split into two different beams, one beam is directed toward a flat reflective surface inside the equipment and the second beam will be directed toward the sample. The reflected beam from the sample will be combined with the reflected beam from the known flat surface and by using the interference patterns in the recombined beam the height profile of the sample can be determined. Examples of optical profilometry measurements are presented in the next chapter.

18

2.4 Infrared Camera for Temperature Measurement

We have controlled the temperature of the samples by using a copper heater. For all our samples, we have designed an uncoated PDMS region that was used as a reference material to define the surface temperature of the sample.[46] The temperature was measured by a calibrated mid-IR camera (T450sc, FLIR). The thick layer of PDMS (>0.2 mm) shows less than 1% transmission for the spectral range of the camera (7.5–13 μm). This fact justifies that PDMS can be used as reference material for temperature measurement. Figure 11 shows a sample infrared image of our blackbody source from our camera, the bright circular spot in the center of the image is the opening of the blackbody.
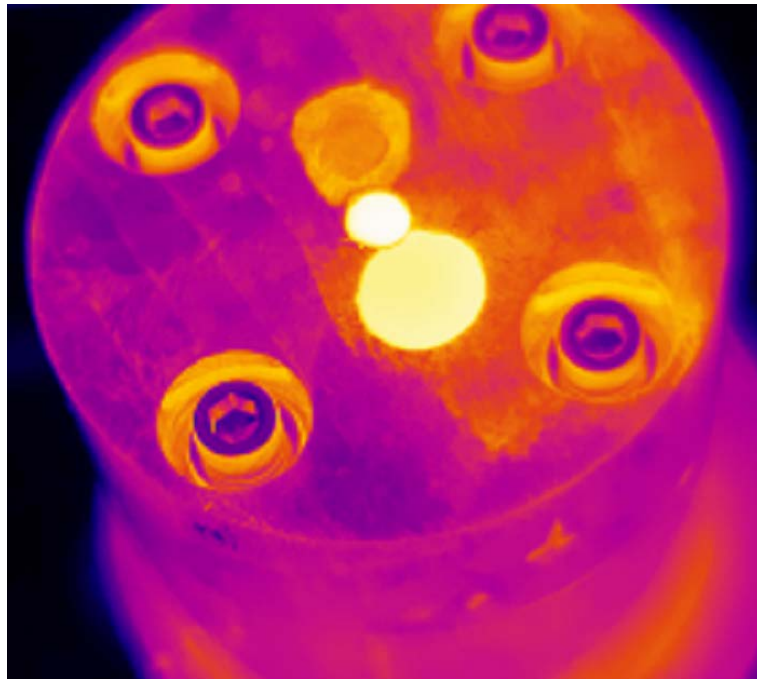
Figure 11- Thermal image of the blackbody with the infrared camera

CHAPTER 3

RESULTS

Due to the necessary tilt to avoid artifacts and given that our samples are highly reflective, the measured radiation includes the thermal radiation reflected from the surroundings of the measurement setup. This grey-body-like radiation contribution should be calculated and removed from the measured radiation for assessing the thermal radiation from the samples. Using a similar approach to calibration of the system, the reflection contribution can be determined by measuring the radiation of the samples at two different temperatures. The reflected radiation from the surroundings does not depend on the temperature of the sample. The radiation of the sample can be described as emissivity times the blackbody radiation at that temperature, assuming a constant emissivity within the measured temperature range. We can then calculate the reflection contribution and the emissivity of the sample using Equation (15):

$$R(\lambda, T) = BG(\lambda) + \varepsilon(\lambda)BB(\lambda, T) \tag{15}$$

This model equation is written for the total measured radiation. In this equation R, BG, ε and BB respectively show the total radiation, the reflected background radiation, the emissivity of the sample, and the blackbody radiation at a temperature T. This model was also verified by measuring the radiation at three different temperatures then choosing different pairs of spectra for the calculation of emissivity and the background radiation.

20

Agreement between calculated emissivity and background spectra have proved the validity of the assumptions in this model.

Polarization of the radiation enhancement is a very important feature and helps with the identification and understanding of physical phenomena. In order to study the polarization of enhanced radiation from our samples, we have used a linear infrared polarizer to measure the radiation of the samples at two perpendicular polarizations that are determined based on the geometrical feature of the samples.

The need for tilting the samples to avoid artifacts caused by reflection has been mentioned in the previous chapter. Samples can be tilted either in the plane defined by the grating lines and the normal to the surface of the samples, or a plane that is defined with a perpendicular line to the grating lines and the normal to the surface of the sample. In the experiments for the next section (3.1), all the tilts are in the second configuration (as opposed to all the other measurements) so that it can be easily simulated.

In all the presented radiation or emissivity spectra, the noise-like features at the short wavelength end of the graphs are due to low signals from samples at low-temperatures in the short wavelength. Depending on the humidity on the day of the measurements, some of the spectra may show several absorption peaks in the 6 to 8 micron range that are due to the water vapor in the air.

21

3.1 Angle-dependency of surface plasmon resonance

To establish the measurement protocol and verify the capabilities of our system, we have measured the thermal radiation of a 4-µm grating structure made at Watkins group in the Polymer Science and Engineering Department at University of Massachusetts, Amherst. The sample was made using an imprint-planarize-imprint strategy that is previously reported in the literature. [47] It was also gold-coated using a conformal supercritical fluid deposition technique that is also reported in the literature. [48]

The results of profilometry measurements of this sample is shown in Figure 12. The figure shows the profile of four lines and also the zoomed-in view of one of the edges to show that the edges are not vertical. These grating lines have a trapezoidal cross section, with a periodicity of 3.93 µm. The heights of the lines vary from 1.05 to 1.35 µm. The widths of the lines vary from 0.89 to 1.79 µm on average from bottom to top.
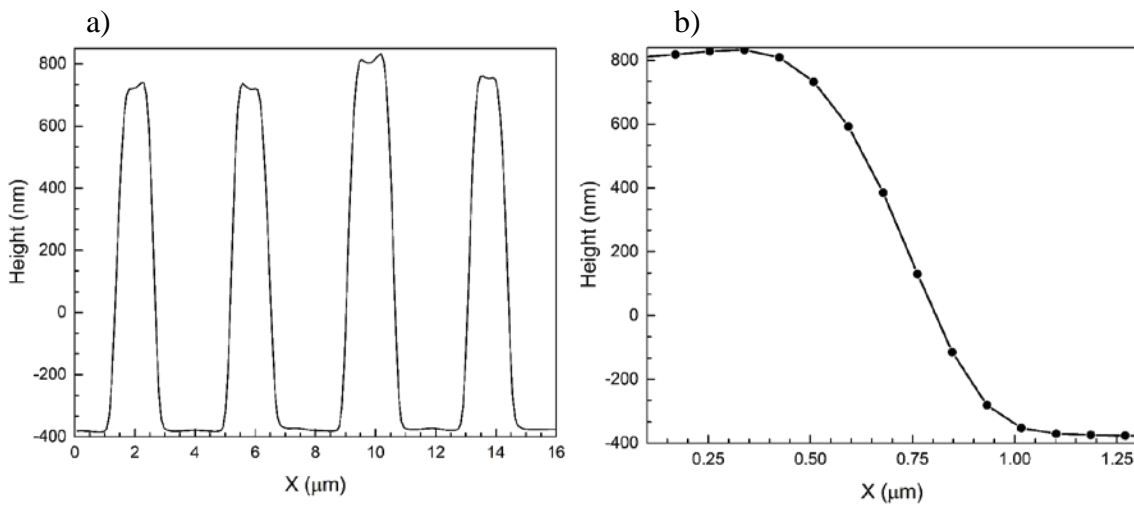
Figure 12- Optical profilometry measurements for the grating sample. a) height profile of 4 grating lines, b) the edge of one of the lines as an example

As a proof for the proposed model presented for emissivity calculation, the radiation of the sample for 7° tilt angle has been measured at 4 different temperatures and the calculations based on two different temperature pairs are shown in Figure 13. The agreement between the emissivity and the background radiation calculation for different temperature sets shows that the proposed model is valid for our applications. The background radiation is very close to a grey-body spectrum at room temperature with emissivity of about 0.9.
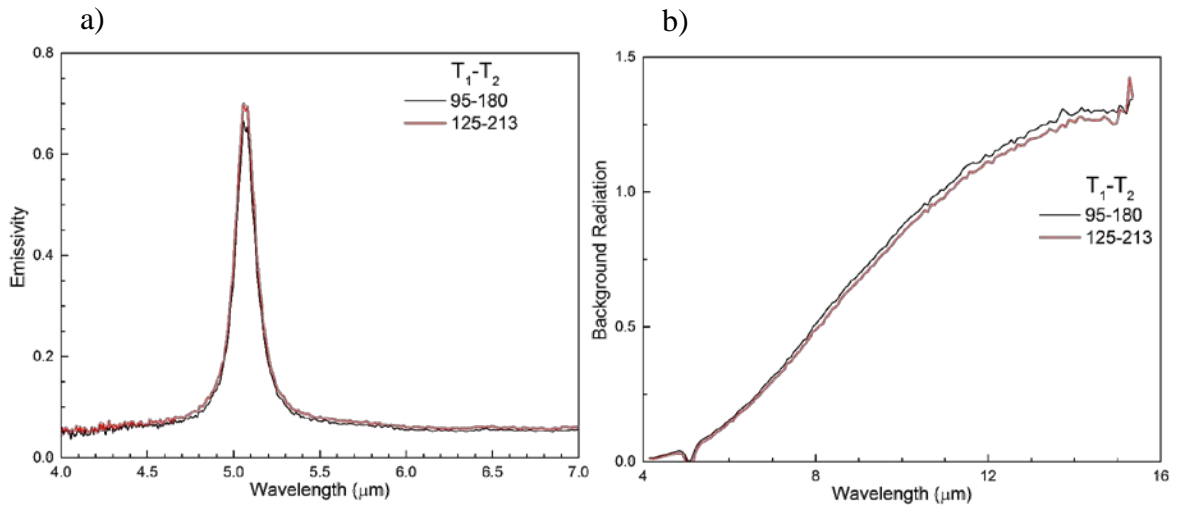
Figure 13- a) Emissivity and b) background radiation spectrum based on the proposed model at different temperature sets.

The Zhang group in the Mechanical Engineering Department at Georgia Institute of Technology has developed a free Rigorous Coupled-Wave Analysis (RCWA) MATLAB package [49] that have been used for simulation of radiation enhancement of the grating structures.
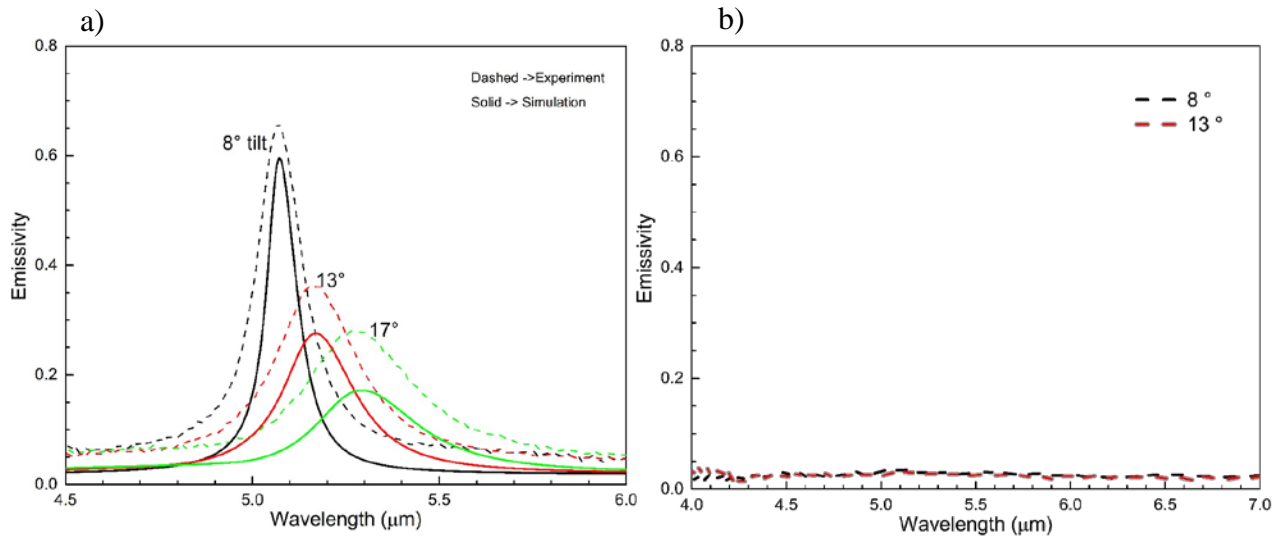
Figure 14- Emissivity of the 4-micron grating structure in a) perpendicular and b) parallel polarizations with respect to the grating lines

The emissivity curves of the sample, measured at two different polarizations, are shown in Figure 14. In our radiometry setup, the radiation is measured within an acceptance angle of 8 degrees i.e. a cone in 3D with vertex angle of 8°. The radiation measurement inside a cone effectively means that detected radiation is an averaged value of emitted radiation in an angle interval of 8 degrees. The RCWA package can determine the spectral radiance for an infinitesimally small solid angle. To make the simulations more accurate,

the emissivity spectra for 16 different angles (0.5° steps) have been calculated and all the spectra were averaged to represent the measurement for an acceptance angle of 8 degrees. Given the complex effects of the cross-section, height, and the width of the grating lines on the wavelength of the enhancements, the first emissivity spectrum was used as a calibration dataset to find the dimensions of an ideal grating structure (height = 1.36 μm, width = 0.96 μm, periodicity = 3.93 μm) for the simulation package that would result in the same peak wavelength for the enhancement. The same dimensions have been used for calculation of the emissivity spectra for the other two measurements. The peak wavelengths from the simulations' results show a good agreement with the experimental measurements.

This enhancement in radiation has been previously studied[50] and is attributed to the coupling of surface waves, surface-plasmon polaritons in this case, and propagating modes by means of the grating on the interface. The enhancements are observed to be highly polarized and very directional. Our measurements do not show the extreme directionality due to measuring the radiation inside a cone and the deviation of the structure from the ideal grating structure.

25

3.2 Tunable Thermal Emitter

The second part of this project was to develop a tunable thermal emitter with very basic fabrication tools. The results of this section has been published in Advanced Optical Materials.[51] The samples were prepared using the strain-induced buckling in the metallic layer which was explained in Chapter 2. The height profiles of the sample are shown in Figure 15.

The samples show cracks in the direction perpendicular to the wrinkles that are caused by the stretch in the metallic layer after relaxation of the elastomeric substrates. The samples show very regular structures throughout the entire coated surface and the amplitude of the structures are proportional to the periodicities of the samples.
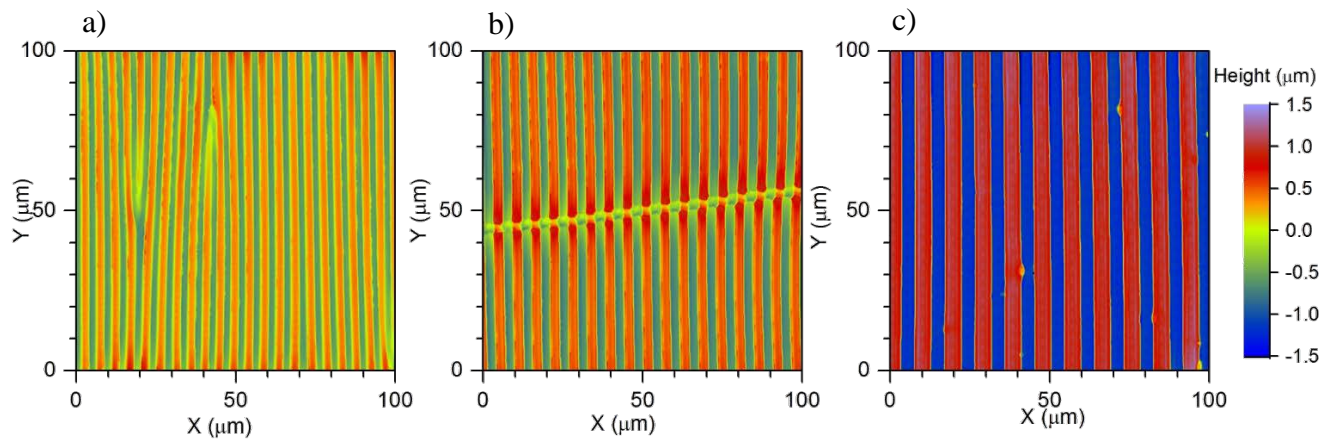
Figure 15 The height profiles of the samples made using strain-induced buckling a) 4.5-micron periodicity b) 6.3-micron periodicity c) 9.4-micron periodicity
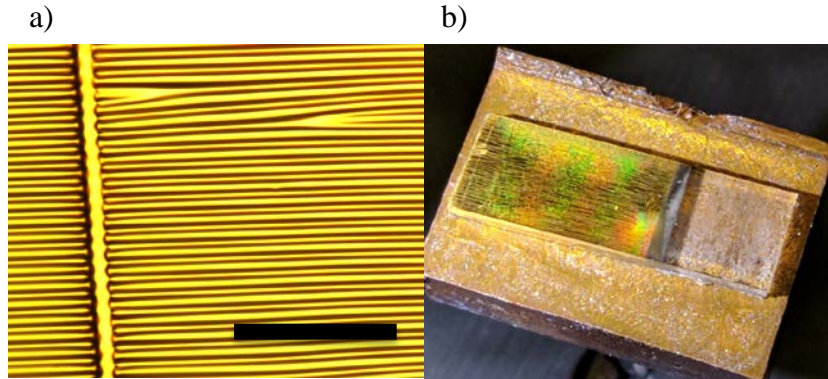
Figure 16- a) Optical images of one sample under reflection microscope (scale bar = 40 micron), b) image of the sample mounted on the heater

The emissivity spectra of these samples for two different polarizations (90° and 0° are respectively polarizations perpendicular and parallel to the direction of grating lines) are shown in Figure 17.
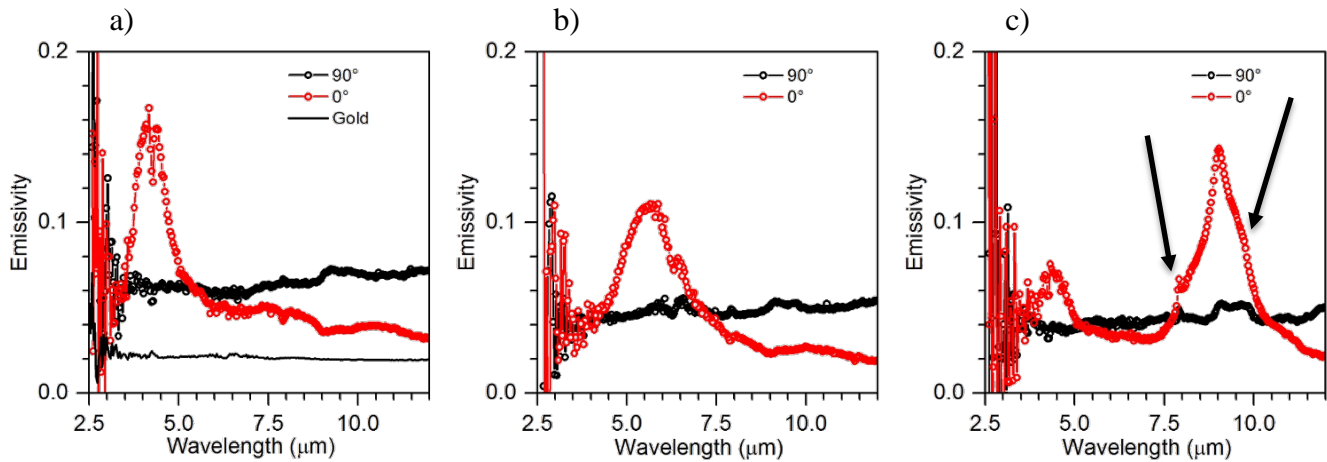
Figure 17- Emissivity spectra for the samples with periodicities of a) 4.5 µm, b) 6.3 µm, and c) 9.4 µm

We have observed that the emissivity of the parallel polarization is higher than emissivity of flat gold because of the larger emitting surface of the wrinkles as compared to a flat surface. We have also observed features that (pointed out by the arrows in Figure 17c) arise from the cracks in the structure where the PDMS substrate, which has

significantly higher emissivity than gold, is not covered by the gold layer. This can be verified by the absorption spectrum of PDMS which is shown in Figure 18 for a 26-μm thick PDMS layer. There is an absorption band in the 9-10 micron range and a strong absorption line at 8 micron, that correspond to the features observed in the emissivity spectra of the wrinkle structure with the periodicity of 9.4 microns.[52], [53]
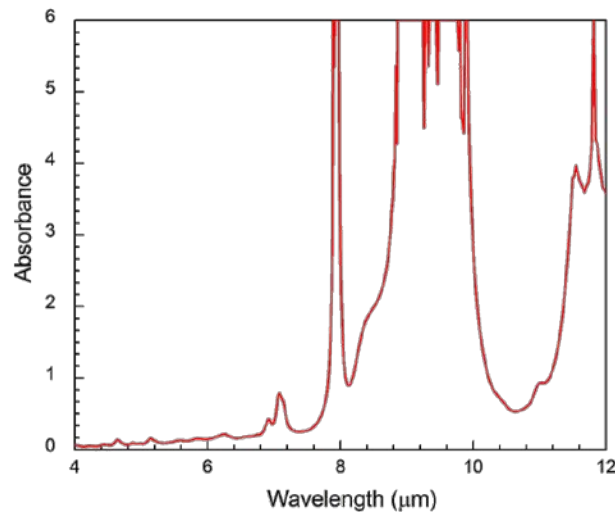
Figure 18- Absorption of PDMS for a 26-micron thick layer

The enhancement peak for the 9.4-micron sample has an unusual shape that can be attributed to indirect plasmonic coupling of through the nickel-gold bilayer.[54]–[56] Surface plasmon polaritons can exist at the interface of metals and dielectric, the nickel-gold bilayer has two interfaces with dielectrics, one interface with air and a second interface with PDMS.[57] If the thickness of the nickel-gold bilayer is thinner than the sum of evanescent amplitudes of surface plasmon polaritons at these two interfaces, the surface waves can couple with each other.[58] This can help explain the unusual shape of the enhancement peak that has features similar to absorption spectrum of PDMS.[59]–[61] We

have also shown the tunability of the thermal radiation enhancement with another sample.

The sample has been stretched and radiation spectra were collected for each stretched step.

The results are shown in Figure 19. Due to an enhancement periodicity close to very strong

PDMS absorption lines, some PDMS characteristic lines are also present in the spectra,[62]

that were explained earlier.
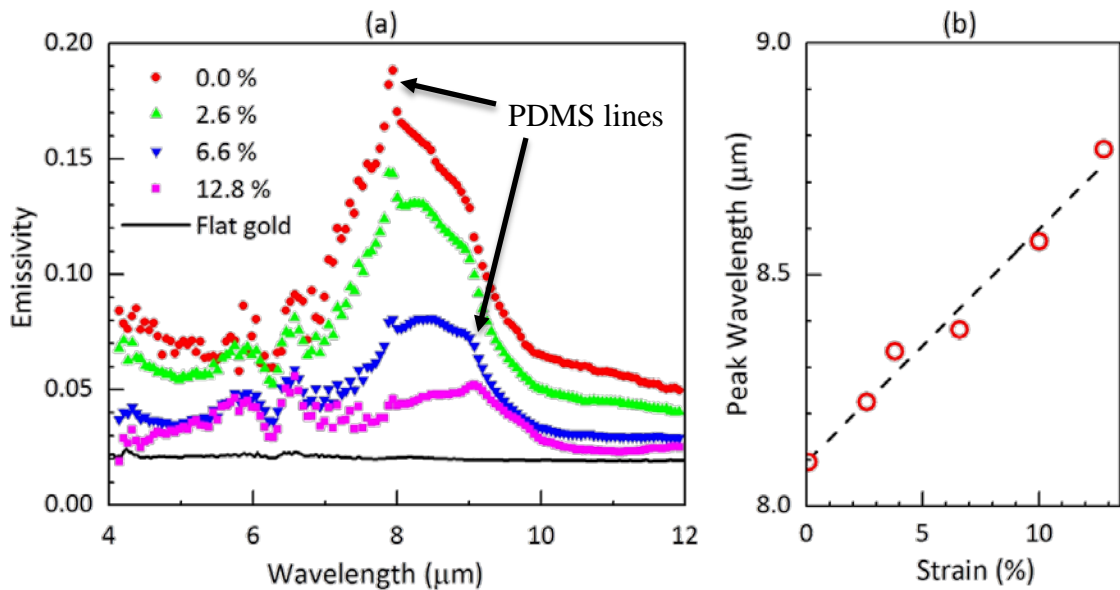
**Figure 19- The shift in the enhancement peak for different strain values. a)
emissivity spectra at different stretched states b) peak wavelength determined using
a Gaussian fit plotted for different strain values**

The vertical shift in the emissivity baseline of the sample supports the idea that was

presented earlier. At higher strain values the surface gets closer to a flat surface which

means the radiative surface per unit area decreases that can explain the vertical shift in the

baseline of the emissivity of the sample.

29

Figure 20 shows an image of the structure that is taken with a scanning electron microscope. A few cracks in the nickel layer are visible in the image and for one of the cracks the PDMS substrate is exposed. This can be explained by the effects of thermal expansion when the sample is heated. The PDMS can break the thin gold layer that is covering the crack. This effect can also contribute to higher baseline emissivity values and the presence of PDMS emission peaks in the measured radiation.
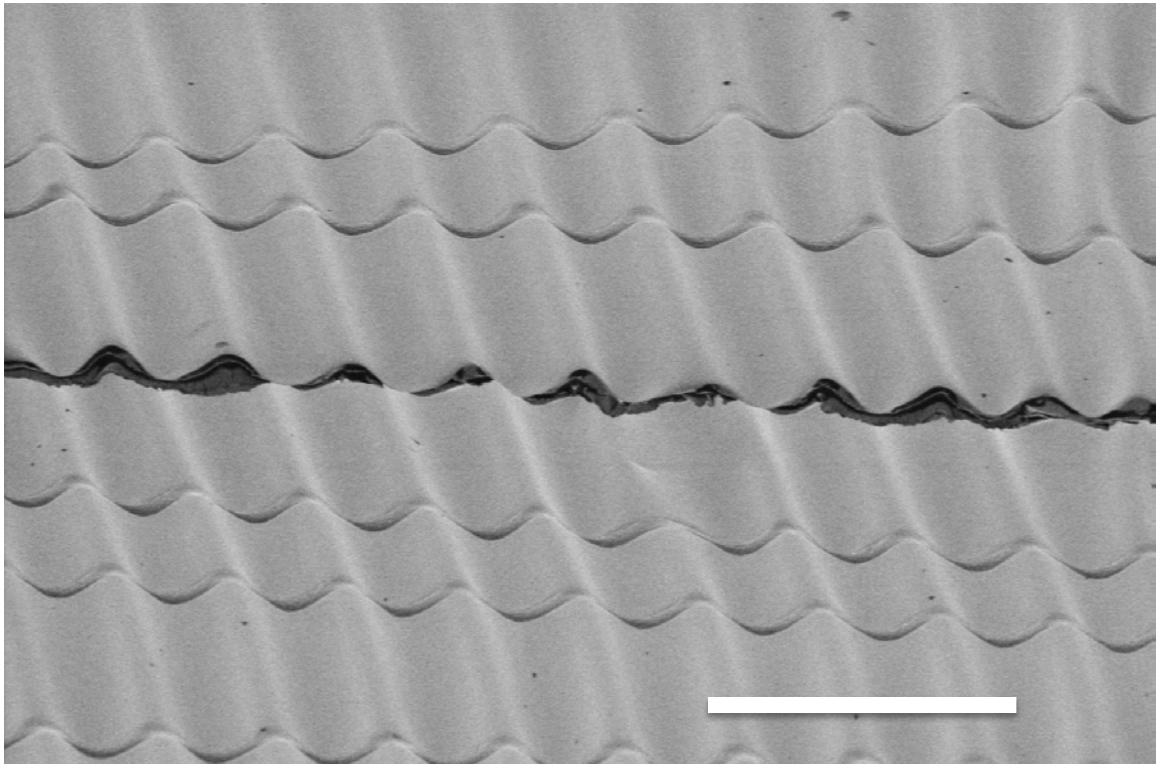
Figure 20- SEM image of the structure, (scale bar = 20 μm)

3.3 Woodpile 3D Thermal Emitter

The last set of samples that we have studied was for a collaborative project with the Watkins group in the Polymer Science and Engineering Department. The results of this work has been published in the American Chemical Society journal of Applied Materials and Interfaces. [48] TiO_2 woodpile structures were fabricated on silicon wafers using an imprint-planarize-imprint strategy. Each layer of patterned TiO_2 was imprinted in a glove box. The TiO_2 nanoparticle dispersion was spin-coated on the substrate and the PDMS stamp was gently placed onto the TiO_2 coating immediately afterwards. The stamped substrate was then placed on a 50 °C hot plate for 6 h before the stamp was peeled off. This sample was then coated with gold using a supercritical fluid coating technique. The cross-section profiles of the top and bottom layer as well as a SEM image of the sample are shown in Figure 21. The bright layer covering the structure shows the conformal coating of gold that covers the entire surface of the sample.
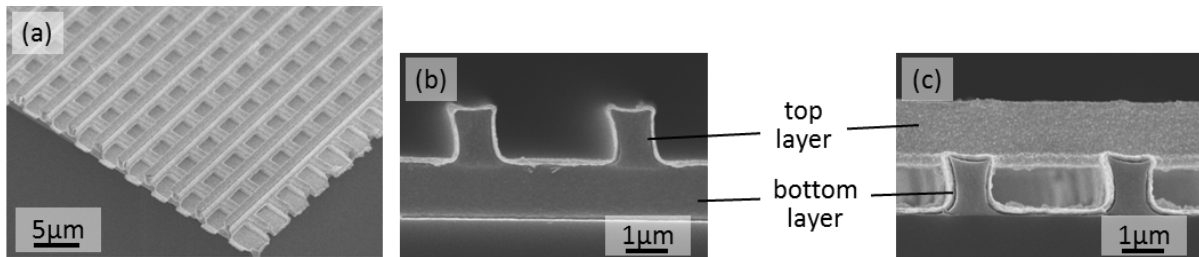
Figure 21- SEM images of 3D woodpile structure. a) the 2-layer woodpile structure imaged at an angle. b) cross-section of the top layer. c) Cross section of the bottom layer

Photonic crystals show stronger radiation enhancement that are only partially polarized.[63]–[66] The enhancement gets stronger with a larger number of layers but can also be detected with only two layers. As the samples should be tilted for radiation measurement to avoid reflection artifacts, completely polarized enhancement peaks that do not originate in the 3D structure of the sample have also been observed. The emissivity spectrum of the sample is shown in Figure 22a. The peak that is fully polarized originates from the surface waves on the top layer of the structure and the partially polarized emission enhancement is attributed to resonance modes at the photonic band edge and is expected to exist at the same wavelength within a wide detection angle.[63][67] In order to show the partially polarized peak exits in a wide detection angle range, the radiation spectrum of the sample was measured at different tilt angles and the results are also shown in Figure 22b.
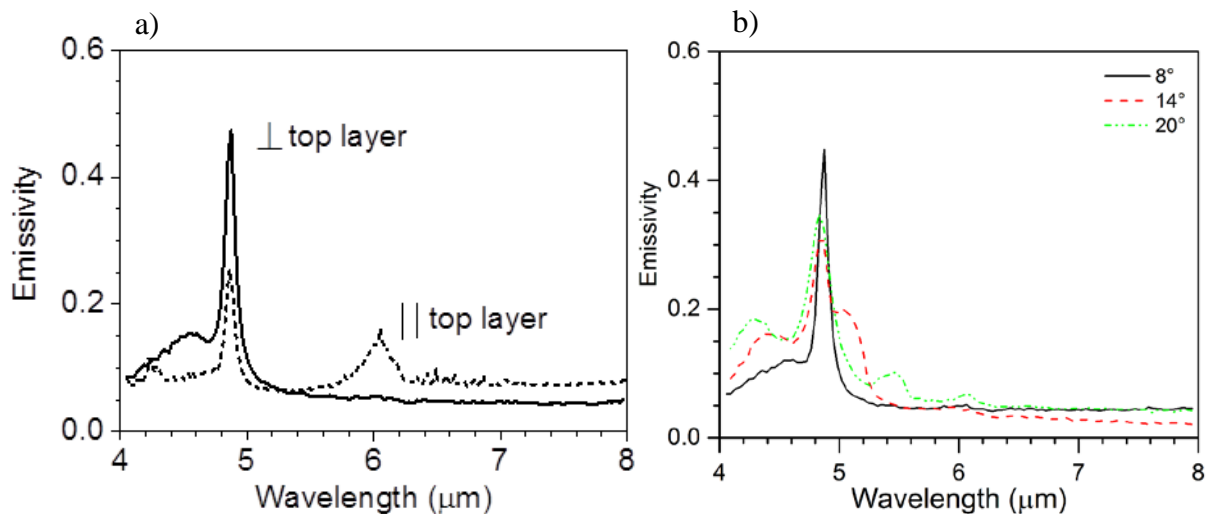
Figure 22- a) Emissivity spectrum of the sample for two polarizations at 8° tilt, b) Emissivity measurement for different tilt angles for perpendicular polarization

The peaks that originate from surface plasmon polariton exhibit strong angle dependency. This fact means that the radiation of those peaks when measured inside a cone will be averaged and broadened and this effect is clear in the peaks on the right and the left of 4.8-micron peak in Figure 22b.[68] The partially polarized peak shows higher locality because the peak wavelength for that peak does not depend on the observation angle.[69]

CHAPTER 4

CONCLUSION AND FUTURE WORK

A thermal radiometry method was established that enables accurate thermal radiation measurement for low- and high- temperature applications. Engineering of mid-IR thermal radiation characteristics was demonstrated with periodic microstructures. Plasmonic thermal emission depended on the structure's periodicity and orientation. The deformable plasmonic thermal emitters can be utilized as strain sensors. We were also able to demonstrate the dynamic modulation of thermal signature of the deformable plasmonic structures, which is potentially advantageous in defense applications. For large-scale plasmonic thermal emitters, aluminum can be considered as a low-cost alternative material for gold. All of our gold-coated structures exhibited significant thermal emission enhancements. This wavelength-selective enhancement is of great utility for thermal photovoltaics and self-cooling devices. This method can be a very useful tool for assessing the potential application of innovative and novel microstructures for industrial, defense and energy applications.

34

BIBLIOGRAPHY

[1]   P. T. Worthing and W. L. Barnes, "Efficient coupling of surface plasmon polaritons to radiation using a bi-grating," *Appl. Phys. Lett.*, vol. 79, no. 19, pp. 3035–3037, 2001.

[2]   S. C. Kitson, W. L. Barnes, and J. R. Sambles, "Full Photonic Band Gap for Surface Modes in the Visible," *Phys. Rev. Lett.*, vol. 77, no. 13, pp. 2670–2673, Sep. 1996.

[3]   A. Tredicucci, C. Gmachl, F. Capasso, A. L. Hutchinson, D. L. Sivco, and A. Y. Cho, "Single-mode surface-plasmon laser," *Appl. Phys. Lett.*, vol. 76, no. 16, pp. 2164–2166, 2000.

[4]   N. Fang, Z. Liu, T.-J. Yen, and X. Zhang, "Regenerating evanescent waves from a silver superlens," *Opt. Express*, vol. 11, no. 7, pp. 682–687, 2003.

[5]   W. L. Barnes, A. Dereux, and T. W. Ebbesen, "Surface plasmon subwavelength optics," *Nature*, vol. 424, p. 824, Aug. 2003.

[6]   W. L. Barnes, "Surface plasmon–polariton length scales: a route to sub-wavelength optics," *J. Opt. A Pure Appl. Opt.*, vol. 8, no. 4, p. S87, 2006.

[7]   A. Polman, "Plasmonics Applied," *Science (80-.).*, vol. 322, no. 5903, p. 868 LP-869, Nov. 2008.

[8]   T. W. Ebbesen, C. Genet, and S. I. Bozhevolnyi, "Surface-plasmon circuitry," *Phys. Today*, vol. 61, no. 5, pp. 44–50, May 2008.

[9]   P. Törmä and W. L. Barnes, "Strong coupling between surface plasmon polaritons and emitters: a review," *Reports Prog. Phys.*, vol. 78, no. 1, p. 13901, 2015.

[10]   S. Lal, S. Link, and N. J. Halas, "Nano-optics from sensing to waveguiding," *Nat. Photonics*, vol. 1, p. 641, Nov. 2007.

[11]   W.-C. Tan, T. W. Preist, J. R. Sambles, and N. P. Wanstall, "Flat surface-plasmon-polariton bands and resonant optical absorption on short-pitch metal gratings," *Phys. Rev. B*, vol. 59, no. 19, pp. 12661–12666, May 1999.

[12]   M.-W. Tsai, T.-H. Chuang, C.-Y. Meng, Y.-T. Chang, and S.-C. Lee, "High performance midinfrared narrow-band plasmonic thermal emitter," *Appl. Phys. Lett.*, vol. 89, no. 17, p. 173116, Oct. 2006.

[13]   T. Inoue, M. De Zoysa, T. Asano, and S. Noda, "Realization of dynamic thermal emission control," *Nat. Mater.*, vol. 13, p. 928, Jul. 2014.

[14] B. W. Carroll and D. A. Ostlie, *An introduction to modern astrophysics*. Cambridge University Press, 2017.

[15] A. V Zayats, I. I. Smolyaninov, and A. A. Maradudin, "Nano-optics of surface plasmon polaritons," *Phys. Rep.*, vol. 408, no. 3, pp. 131–314, 2005.

[16] S. A. Maier, *Plasmonics: Fundamentals and applications*. 2007.

[17] J. M. Pitarke, V. M. Silkin, E. V Chulkov, and P. M. Echenique, "Theory of surface plasmons and surface-plasmon polaritons," *Reports Prog. Phys.*, vol. 70, no. 1, p. 1, 2007.

[18] S. A. Maier and H. A. Atwater, "Plasmonics: Localization and guiding of electromagnetic energy in metal/dielectric structures," *J. Appl. Phys.*, vol. 98, no. 1, p. 11101, Jul. 2005.

[19] S. D. Brorson and H. A. Haus, "Diffraction gratings and geometrical optics," *J. Opt. Soc. Am. B*, vol. 5, no. 2, pp. 247–248, 1988.

[20] M. U. Pralle *et al.*, "Photonic crystal enhanced narrow-band infrared emitters," *Appl. Phys. Lett.*, vol. 81, no. 25, pp. 4685–4687, Dec. 2002.

[21] W. L. Barnes, T. W. Preist, S. C. Kitson, and J. R. Sambles, "Physical origin of photonic energy gaps in the propagation of surface plasmons on gratings," *Phys. Rev. B*, vol. 54, no. 9, pp. 6227–6244, Sep. 1996.

[22] T. W. Ebbesen, H. J. Lezec, H. F. Ghaemi, T. Thio, and P. A. Wolff, "Extraordinary optical transmission through sub-wavelength hole arrays," *Nature*, vol. 391, p. 667, Feb. 1998.

[23] S. C. Kitson, W. L. Barnes, and J. R. Sambles, "Surface-plasmon energy gaps and photoluminescence," *Phys. Rev. B*, vol. 52, no. 15, pp. 11441–11445, Oct. 1995.

[24] A. Giannattasio and W. L. Barnes, "Direct observation of surface plasmon-polariton dispersion," *Opt. Express*, vol. 13, no. 2, pp. 428–434, 2005.

[25] N. Bowden, S. Brittain, A. G. Evans, J. W. Hutchinson, and G. M. Whitesides, "Spontaneous formation of ordered structures in thin films of metals supported on an elastomeric polymer," *Nature*, vol. 393, p. 146, May 1998.

[26] C. M. Stafford *et al.*, "A buckling-based metrology for measuring the elastic moduli of polymeric thin films," *Nat. Mater.*, vol. 3, p. 545, Jul. 2004.

[27] A. L. Volynskii, S. Bazhenov, O. V Lebedeva, and N. F. Bakeev, "Mechanical buckling instability of thin coatings deposited on soft polymer substrates," *J. Mater. Sci.*, vol. 35, no. 3, pp. 547–554, Feb. 2000.

[28] J. J. Talghader, A. S. Gawarikar, and R. P. Shea, "Spectral selectivity in infrared thermal detection," *Light Sci. &Amp; Appl.*, vol. 1, p. e24, Aug. 2012.

[29] R. Stanley, "Plasmonics in the mid-infrared," *Nat. Photonics*, vol. 6, p. 409, Jun. 2012.

[30] X. Liu, T. Tyler, T. Starr, A. F. Starr, N. M. Jokerst, and W. J. Padilla, "Taming the Blackbody with Infrared Metamaterials as Selective Thermal Emitters," *Phys. Rev. Lett.*, vol. 107, no. 4, p. 45901, Jul. 2011.

[31] J. A. Mason, S. Smith, and D. Wasserman, "Strong absorption and selective thermal emission from a midinfrared metamaterial," *Appl. Phys. Lett.*, vol. 98, no. 24, p. 241105, Jun. 2011.

[32] M. Jackson and H. H. Mantsch, "The Use and Misuse of FTIR Spectroscopy in the Determination of Protein Structure," *Crit. Rev. Biochem. Mol. Biol.*, vol. 30, no. 2, pp. 95–120, Jan. 1995.

[33] Z. Movasaghi, S. Rehman, and D. I. ur Rehman, "Fourier Transform Infrared (FTIR) Spectroscopy of Biological Tissues," *Appl. Spectrosc. Rev.*, vol. 43, no. 2, pp. 134–179, Feb. 2008.

[34] "Nicolet 6700 User's Manual." [Online]. Available: https://instrumentalanalysis.community.uaf.edu/files/2013/01/FT-IR_manual.pdf.

[35] P. R. Griffiths and J. A. De Haseth, *Fourier transform infrared spectrometry*, vol. 171. John Wiley & Sons, 2007.

[36] "Nicolet 6700 Borchure."

[37] R. E. Shaffer, G. W. Small, R. J. Combs, R. B. Knapp, and R. T. Kroutil, "Experimental design protocol for the pattern recognition analysis of bandpass filtered Fourier transform infrared interferograms," *Chemom. Intell. Lab. Syst.*, vol. 29, no. 1, pp. 89–108, 1995.

[38] G. W. Small, S. E. Carpenter, T. F. Kaltenbach, and R. T. Kroutil, "Discriminant analysis techniques for the identification of atmospheric pollutants from passive Fourier transform infrared interferograms," *Anal. Chim. Acta*, vol. 246, no. 1, pp. 85–102, 1991.

[39] W. Herres and J. Gronholz, "Understanding FT· IR Data Processing."

[40] P. Werle, F. Slemr, K. Maurer, R. Kormann, R. Mücke, and B. Jänker, "Near- and mid-infrared laser-optical sensors for gas analysis," *Opt. Lasers Eng.*, vol. 37, no. 2, pp. 101–114, 2002.

[41] J. Mulrooney, J. Clifford, C. Fitzpatrick, and E. Lewis, "Detection of carbon dioxide emissions from a diesel engine using a mid-infrared optical fibre based sensor," *Sensors Actuators A Phys.*, vol. 136, no. 1, pp. 104–110, 2007.

[42] K. D. Kempfert, E. Y. Jiang, S. Oas, and J. Coffin, "Detectors for Fourier transform spectroscopy."

[43] A. Rogalski, "HgCdTe infrared detector material: history, status and outlook," *Reports Prog. Phys.*, vol. 68, no. 10, p. 2267, 2005.

[44] P. de Groot and L. Deck, "Surface Profiling by Analysis of White-light Interferograms in the Spatial Frequency Domain," *J. Mod. Opt.*, vol. 42, no. 2, pp. 389–401, Feb. 1995.

[45] P. Sandoz, G. Tribillon, and H. Perrin, "High-resolution profilometry by using phase calculation algorithms for spectroscopic analysis of white-light interferograms," *J. Mod. Opt.*, vol. 43, no. 4, pp. 701–708, Apr. 1996.

[46] Z. M. Zhang, B. K. Tsai, and G. Machin, *Radiometric Temperature Measurements: II. Applications*, vol. 43. Academic Press, 2009.

[47] R. Kothari, M. R. Beaulieu, N. R. Hendricks, S. Li, and J. J. Watkins, "Direct Patterning of Robust One-Dimensional, Two-Dimensional, and Three-Dimensional Crystalline Metal Oxide Nanostructures Using Imprint Lithography and Nanoparticle Dispersion Inks," *Chem. Mater.*, vol. 29, no. 9, pp. 3908–3918, 2017.

[48] S. Li *et al.*, "Wavelength-Selective Three-Dimensional Thermal Emitters via Imprint Lithography and Conformal Metallization," *ACS Appl. Mater. Interfaces*, vol. 10, no. 9, pp. 8173–8179, 2018.

[49] B. Zhao and Z. Zhang, "RCWA Package," 2014.

[50] J.-J. Greffet, R. Carminati, K. Joulain, J.-P. Mulet, S. Mainguy, and Y. Chen, "Coherent emission of light by thermal sources," *Nature*, vol. 416, p. 61, Mar. 2002.

[51] K. M. Amir, Z. Robert, X. Wanting, H. Irene, W. J. J., and L. Jae-Hwang, "Plasmonic Thermal Emitters for Dynamically Tunable Infrared Radiation," *Adv. Opt. Mater.*, vol. 5, no. 10, p. 1600993.

[52] C. E. Petoukhoff and D. M. O'Carroll, "Absorption-induced scattering and surface plasmon out-coupling from absorber-coated plasmonic metasurfaces," *Nat. Commun.*, vol. 6, p. 7899, Aug. 2015.

[53]   R. Adato, A. Artar, S. Erramilli, and H. Altug, "Engineered Absorption Enhancement and Induced Transparency in Coupled Molecular and Plasmonic Resonator Systems," *Nano Lett.*, vol. 13, no. 6, pp. 2584–2591, Jun. 2013.

[54]   A. Giannattasio, I. R. Hooper, and W. L. Barnes, "Transmission of light through thin silver films via surface plasmon-polaritons," *Opt. Express*, vol. 12, no. 24, pp. 5881–5886, 2004.

[55]   S. Wedge and W. L. Barnes, "Surface plasmon-polariton mediated light emission through thin metal films," *Opt. Express*, vol. 12, no. 16, pp. 3673–3685, 2004.

[56]   S. N. JASPERSON and S. E. SCHNATTERLY, "Photon-Surface-Plasmon Coupling in Thick Ag Foils," *Phys. Rev.*, vol. 188, no. 2, pp. 759–770, Dec. 1969.

[57]   W. L. Barnes, W. A. Murray, J. Dintinger, E. Devaux, and T. W. Ebbesen, "Surface Plasmon Polaritons and Their Role in the Enhanced Transmission of Light through Periodic Arrays of Subwavelength Holes in a Metal Film," *Phys. Rev. Lett.*, vol. 92, no. 10, p. 107401, Mar. 2004.

[58]   P. Andrew and W. L. Barnes, "Energy Transfer Across a Metal Film Mediated by Surface Plasmon Polaritons," *Science (80-.).*, vol. 306, no. 5698, p. 1002 LP-1005, Nov. 2004.

[59]   N. T. Fofang, T.-H. Park, O. Neumann, N. A. Mirin, P. Nordlander, and N. J. Halas, "Plexcitonic Nanoparticles: Plasmon−Exciton Coupling in Nanoshell−J-Aggregate Complexes," *Nano Lett.*, vol. 8, no. 10, pp. 3481–3487, Oct. 2008.

[60]   M. Ambati, S. H. Nam, E. Ulin-Avila, D. A. Genov, G. Bartal, and X. Zhang, "Observation of Stimulated Emission of Surface Plasmon Polaritons," *Nano Lett.*, vol. 8, no. 11, pp. 3998–4001, Nov. 2008.

[61]   T. D. Neal, K. Okamoto, A. Scherer, M. S. Liu, and A. K.-Y. Jen, "Time resolved photoluminescence spectroscopy of surface-plasmon-enhanced light emission from conjugate polymers," *Appl. Phys. Lett.*, vol. 89, no. 22, p. 221106, Nov. 2006.

[62]   B. Park *et al.*, "Surface plasmon excitation in semitransparent inverted polymer photovoltaic devices and their applications as label-free optical sensors," *Light Sci. &Amp; Appl.*, vol. 3, p. e222, Dec. 2014.

[63]   L. Jae-Hwang *et al.*, "Polarization Engineering of Thermal Radiation Using Metallic Photonic Crystals," *Adv. Mater.*, vol. 20, no. 17, pp. 3244–3247.

[64]   G. F., X. M., L. V., F. S., B. P. V., and L. J. A., "A Germanium Inverse Woodpile Structure with a Large Photonic Band Gap," *Adv. Mater.*, vol. 19, no. 12, pp. 1567–1570, May 2007.

[65] S. R. Huisman, R. V Nair, L. A. Woldering, M. D. Leistikow, A. P. Mosk, and W. L. Vos, "Signature of a three-dimensional photonic band gap observed on silicon inverse woodpile photonic crystals," *Phys. Rev. B*, vol. 83, no. 20, p. 205313, May 2011.

[66] G. Subramania, Y.-J. Lee, I. Brener, T. S. Luk, and P. G. Clem, "Nano-lithographically fabricated titanium dioxide based visible frequency three dimensional gap photonic crystal," *Opt. Express*, vol. 15, no. 20, pp. 13049–13057, 2007.

[67] L. J.-H., K. Y.-S., C. K., and H. K.-M., "Woodpile Metallic Photonic Crystals Fabricated by Using Soft Lithography for Tailored Thermal Emission," *Adv. Mater.*, vol. 19, no. 6, pp. 791–794, 2006.

[68] B. Luk'yanchuk *et al.*, "The Fano resonance in plasmonic nanostructures and metamaterials," *Nat. Mater.*, vol. 9, p. 707, Aug. 2010.

[69] J.-H. Lee, C.-H. Kim, Y.-S. Kim, K.-M. Ho, K. Constant, and C. H. Oh, "Three-dimensional metallic photonic crystals fabricated by soft lithography for midinfrared applications," *Appl. Phys. Lett.*, vol. 88, no. 18, p. 181112, 2006.